ANOMALOUS CO$_2$ ICE TOWARD HOPS-68: A TRACER OF PROTOSTELLAR FEEDBACK

Charles A. Poteet[1,6], Klaus M. Pontoppidan[2], S. Thomas Megeath[1], Dan M. Watson[3], Karoliina Isokoski[4],
Jon E. Bjorkman[1], Patrick D. Sheehan[3,5], and Harold Linnartz[4]

[1] Department of Physics and Astronomy, The University of Toledo, 2801 West Bancroft Street, Toledo, OH 43606, USA; charles.poteet@gmail.com
[2] Space Telescope Science Institute, 3700 San Martin Drive, Baltimore, MD 21218, USA
[3] Department of Physics and Astronomy, University of Rochester, Rochester, NY 14627, USA
[4] Sackler Laboratory for Astrophysics, Leiden Observatory, Leiden University, P.O. Box 9513, 2300 RA Leiden, The Netherlands
[5] Steward Observatory, University of Arizona, 933 North Cherry Avenue, Tucson, AZ 85721, USA

ABSTRACT

We report the detection of a unique CO$_2$ ice band toward the deeply embedded, low-mass protostar HOPS-68. Our spectrum, obtained with the Infrared Spectrograph on board the *Spitzer Space Telescope*, reveals a 15.2 μm CO$_2$ ice bending mode profile that cannot be modeled with the same ice structure typically found toward other protostars. We develop a modified CO$_2$ ice profile decomposition, including the addition of new high-quality laboratory spectra of pure, crystalline CO$_2$ ice. Using this model, we find that 87%–92% of the CO$_2$ is sequestered as spherical, CO$_2$-rich mantles, while typical interstellar ices show evidence of irregularly shaped, hydrogen-rich mantles. We propose that (1) the nearly complete absence of unprocessed ices along the line of sight is due to the flattened envelope structure of HOPS-68, which lacks cold absorbing material in its outer envelope, and possesses an extreme concentration of material within its inner (10 AU) envelope region and (2) an energetic event led to the evaporation of inner envelope ices, followed by cooling and re-condensation, explaining the sequestration of spherical, CO$_2$ ice mantles in a hydrogen-poor mixture. The mechanism responsible for the sublimation could be either a transient accretion event or shocks in the interaction region between the protostellar outflow and envelope. The proposed scenario is consistent with the rarity of the observed CO$_2$ ice profile, the formation of nearly pure CO$_2$ ice, and the production of spherical ice mantles. HOPS-68 may therefore provide a unique window into the protostellar feedback process, as outflows and heating shape the physical and chemical structure of protostellar envelopes and molecular clouds.

Key words: astrochemistry – circumstellar matter – methods: laboratory – stars: formation – stars: individual (HOPS-68, FIR-2) – stars: protostars

Online-only material: color figures

1. INTRODUCTION

Stars form in cores deeply embedded within dense molecular clouds by gravitational collapse. As an inseparable part of the star formation process, released gravitational energy from the central protostar heats the surrounding infalling envelope, and angular momentum is shedded via powerful bipolar outflows. These feedback mechanisms serve to disperse protostellar envelopes, halt further accretion, and sculpt the physical and chemical properties of star-forming regions, ultimately contributing to the evolution and destruction of their environment and the generation of turbulence (e.g., McKee & Ostriker 2007). Understanding the feedback loop between protostars and molecular clouds is challenging, in part because protostellar evolution is a stochastic process where violent accretion events may punctuate periods of more moderate accretion (Hartmann & Kenyon 1996; Dunham & Vorobyov 2012; Fischer et al. 2012). Hence, most observations of any given protostar only provide a single evolutionary snapshot, potentially leading to a biased interpretation. As a remedy, observers have long sought tracers of the chemical and physical histories of protostars and their environments (Charnley 1997; Arce et al. 2007). One such tracer is CO$_2$ ice.

Since its first detection by the *Infrared Astronomical Satellite* (D'Hendecourt & Jourdain de Muizon 1989), solid CO$_2$ has proven to be an abundant and ubiquitous constituent of the interstellar medium. Observations of the 4.27 and 15.2 μm

vibrational modes toward the Galactic molecular environments of both quiescent dark clouds (Whittet et al. 1998, 2007, 2009; Bergin et al. 2005; Knez et al. 2005) and circumstellar envelopes of low- and high-mass protostars (Gerakines et al. 1999; Nummelin et al. 2001; Boogert et al. 2004; Pontoppidan et al. 2008; Zasowski et al. 2009; Cook et al. 2011) have revealed a solid CO$_2$ abundance of ∼15%–40% with respect to H$_2$O. Chemical models indicate that gas-phase formation of CO$_2$ is highly inefficient at low temperature, and solid CO$_2$ is therefore widely assumed to be produced through chemical reactions on the surfaces of icy grain mantles (Tielens & Hagen 1982). Despite many experimental efforts to investigate the formation routes to solid CO$_2$, the precise chemical pathway is still debated (Roser et al. 2001; Ruffle & Herbst 2001; Mennella et al. 2004; Oba et al. 2010; Noble et al. 2011; Ioppolo et al. 2011; Garrod & Pauly 2011).

The spectral profile of the CO$_2$ bending mode is a sensitive diagnostic of the local molecular environment. In observations toward cold, quiescent molecular clouds, the profile is invariably characterized by a relatively broad, single-peaked, asymmetric absorption profile at 15.2 μm (Knez et al. 2005; Bergin et al. 2005; Whittet et al. 2007). The quiescent profile can generally be modeled as a linear combination of hydrogen-rich (H$_2$O:CO$_2$) and CO-rich (CO:CO$_2$) ice mixtures, typically dominated by the hydrogen-rich component, at low temperatures ($T < 20$ K).

At the other extreme, along lines of sight toward highly luminous ($L \approx 10^4 \, L_\odot$), massive protostars, the bending mode often exhibits a double-peaked substructure near 15.15 and 15.27 μm (Gerakines et al. 1999). The double-peaked substructure is attributed to Davydov splitting, a phenomenon observed in

molecular crystals having more than one equivalent molecule per unit cell (Davydov 1962), and is characteristic of pure, crystalline CO_2 (Ehrenfreund et al. 1997, 1999; van Broekhuizen et al. 2006). The presence of pure CO_2 is generally interpreted as the result of thermal processing of icy grains seen along quiescent lines of sight. Gerakines et al. (1999) modeled the formation of pure CO_2 as a *segregation* process of the hydrogen-rich component, requiring strong heating to high temperatures ($T \approx 100$ K, or close to the desorption temperature of the H_2O ice). Pontoppidan et al. (2008) suggested, by modeling the presence of CO_2 ice toward low-luminosity ($L \approx 1\,L_\odot$) protostars, that pure CO_2 is also produced following the thermal desorption of CO from the CO:CO_2 mixture. This *distillation* process has the advantage that it can occur at much lower temperatures ($T = 20$–30 K). In either case, the band profile of solid CO_2 is an *irreversible* tracer of thermal processing. That is, by observing CO_2 ice, it can be determined whether the molecular cloud material has been heated significantly above ~ 20–30 K, even if it has since re-cooled. As such, past accretion outbursts have recently been invoked to explain the formation of pure CO_2 ice in low-luminosity ($L \lesssim 1\,L_\odot$) protostars (Kim et al. 2012).

Pontoppidan et al. (2008) found that all observed CO_2 bending mode profiles toward protostellar environments can be decomposed, phenomenologically, into five unique components. Through the comparison with laboratory ice analogs, these components are ascribed to pure CO_2 ice, CO_2 mixed with CO or H_2O ice, dilute CO_2 mixed with pure CO ice, and CO_2 mixed with annealed CH_3OH and H_2O ices. Each component has a fixed profile, but their relative column densities vary from source to source, likely reflecting variations in the pristine-to-processed ice fraction along the line of sight. Moreover, this "unique component" structure appears to be a common property of other ice bands formed near protostars (e.g., CO and the 6–8 μm complex; Pontoppidan et al. 2003; Boogert et al. 2008).

There exists, however, at least one exception to the unique component model; in this paper, we demonstrate that the 15.2 μm CO_2 ice band profile observed toward the peculiar protostar, HOPS-68, cannot be modeled with the same CO_2 ice structure that characterizes other protostars. Originally identified as the compact millimeter source FIR-2 (Mezger et al. 1990), the object is located in the Orion Molecular Cloud 2 region (OMC-2; Gatley et al. 1974) at an adopted distance of 414 ± 7 pc (Menten et al. 2007). Poteet et al. (2011) showed that HOPS-68 is a moderately luminous (1.3 $L_\odot$) protostar with a flattened, relatively dense, infalling envelope that is viewed at an intermediate inclination ($\theta \lesssim 41°$). From the observed spectral energy distribution (SED), they estimate a mass infall rate of $\dot{M} = 7.6 \times 10^{-6}\,M_\odot\,\mathrm{yr}^{-1}$.

HOPS-68 is the first protostar to exhibit unambiguous evidence for the presence of crystalline silicates in *absorption* (Poteet et al. 2011), indicating that the silicates in its protostellar envelope have undergone strong thermal processing ($T \gtrsim 1000$ K). While the mechanisms responsible for such processing are still not fully understood, Poteet et al. (2011) proposed that amorphous silicates were annealed or vaporized within the warm inner region of the disk and/or envelope and subsequently transported outward by entrainment in protostellar outflows. Alternatively, an in situ formation by outflow-induced shocks may be responsible for the production of such material. As such, HOPS-68 might offer us a rare window into the effects of outflows on the solid component of protostellar envelopes.

In Section 2, an overview of the spectroscopic observations, data reduction, and optical depth spectra is presented. In Section 3, we demonstrate that the 15.2 μm bending mode profile toward HOPS-68 is anomalous, and derive a new model for the CO_2 ice structure. Finally, in Section 4 we discuss possible physical scenarios that may explain the anomalous CO_2 ice structure toward HOPS-68 in the context for more typical low-mass protostars. The Appendix presents new high-quality laboratory spectra of pure, crystalline CO_2 ice that are deployed in our analysis.

2. THE *SPITZER*-IRS SPECTRUM

2.1. Observations and Data Reduction

A high-resolution 10–37 μm spectrum of HOPS-68 ($\alpha = 05^\mathrm{h}35^\mathrm{m}24\fs30$, $\delta = -05°08'30\farcs6$ [J2000]) was obtained on 2008 November 14 using the *Spitzer Space Telescope* (Werner et al. 2004) Infrared Spectrograph (IRS; Houck et al. 2004). The observations (*Spitzer* AOR 26614016) were performed with the high-resolution ($\lambda/\Delta\lambda \sim 600$) IRS modules, short–high (SH; 9.9–19.6 μm) and long–high (LH; 18.7–37.2 μm), at each of the two nominal nod positions, one-third of the way from the slit ends. The total exposure times were 120 and 240 s in the SH and LH modules, respectively, and were split between on- and off-source sky pointings.

The spectrum was extracted from the Spitzer Science Center S18.7 pipeline basic calibrated data using the SMART software package (Higdon et al. 2004). Permanently bad and "rogue" pixels were identified and corrected for by interpolation over nearby good pixels in the dispersion direction of the two-dimensional image. In order to remove sky emission from the high-resolution data, we averaged the sky observations and subtracted their mean from the on-source data for HOPS-68. The sky-subtracted two-dimensional images were averaged by nod position, and extracted using a full slit extraction. Spectra of Markarian 231 (LH) and α Lac (SH) were produced in the same manner, and relative spectral response functions (RSRFs) were produced by dividing a template by these spectra. Each nod of the HOPS-68 spectrum was then multiplied by these RSRFs to calibrate the flux density scale and the nods were averaged to obtain a final spectrum. Finally, the SH and LH spectra were scaled to the flux density of the second order of the long–low spectrum (LL2; 14.2–20.4 μm) from Poteet et al. (2011). The resultant SH spectrum is shown in the top panel of Figure 1.

2.2. Optical Depth Spectrum

We convert the CO_2 flux density to an optical depth spectrum, using $\tau(\lambda) = -\ln(F_\lambda^\mathrm{obs}/F_\lambda^\mathrm{cont})$, where F_λ^obs and F_λ^cont are the observed and continuum flux densities, respectively. The continuum is constructed by fitting a third-order polynomial to the observed flux density within the wavelength ranges of 13.0–13.3, 14.6–14.7, and 18.2–19.5 μm; the 13.5–14.2 μm range is avoided due to the rare gas-phase absorption of C_2H_2 (13.71 μm) and HCN (14.05 μm). The polynomial is then combined with a Gaussian in the wavenumber domain, with a center at $\tilde{\nu} = 608$ cm^{-1} and an FWHM of $\Delta\tilde{\nu} = 73$ cm^{-1}, to simulate the blue wing of the 18 μm silicate bending mode (Pontoppidan et al. 2008).

3. AN ANOMALOUS CO_2 ICE BAND

The derived CO_2 ice optical depth spectrum of HOPS-68 is presented in the bottom panel of Figure 1. The profile exhibits prominent double-peaked substructure at 15.05 and 15.24 μm, characteristic of pure, crystalline CO_2 ice (Hudgins et al. 1993;
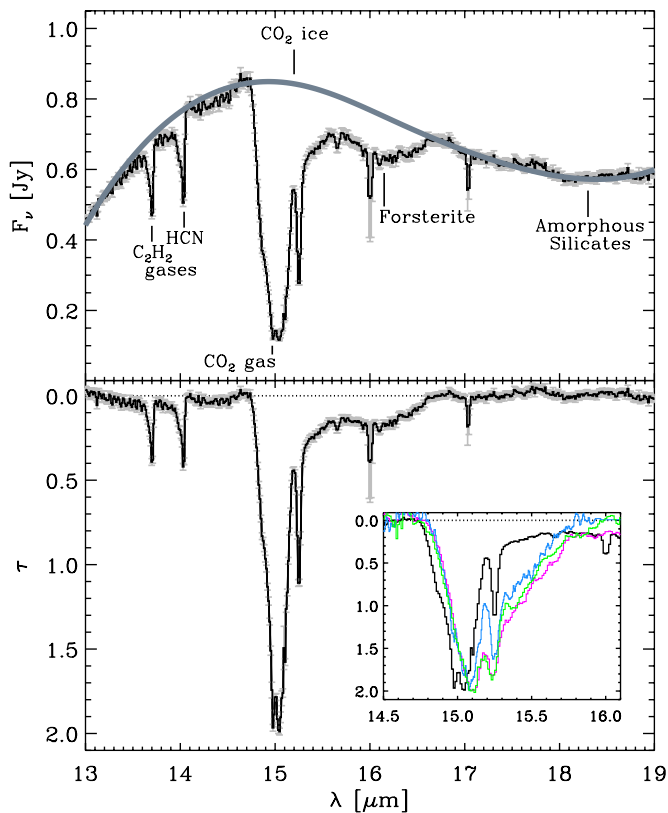
Figure 1. Top panel: *Spitzer*-IRS 13–19 μm SH spectrum of HOPS-68, shown with statistical uncertainties (gray lines) and the adopted continuum (thick gray line). The broad absorption near 16.1 μm has been ascribed to forsterite (Mg$_2$SiO$_4$; Poteet et al. 2011), and the narrow lines at 16.0 and 17.03 μm are background-subtraction artifacts, the latter resulting from H$_2$ S(1) emission near the source. Bottom panel: derived optical depth spectrum of HOPS-68 (black line), centered near the strong 15.2 μm CO$_2$ ice $\tilde{\nu}_2$ bending mode. The sharp absorption feature at 14.97 μm corresponds to the blended Q-branch rovibrational lines of gaseous CO$_2$. Inset: close-up of the 14.5–16 μm spectrum of HOPS-68 (black line), with scaled optical depth profiles from the protostars: S140 IRS 1 (blue line; ×9.0), RNO 91 (green line; ×3.4), and IRAS 03254 (magenta line; ×4.5) shown for comparison.

(A color version of this figure is available in the online journal.)

Ehrenfreund et al. 1997). The CO$_2$ bending mode profiles toward the well-studied protostars S140 IRS 1, RNO 91, and IRAS 03254 are shown for comparison in the inset of Figure 1, illustrating that the HOPS-68 profile is fundamentally different (Pontoppidan et al. 2008; Gerakines et al. 1999). The double-peaked substructure toward these low- and high-mass protostars occurs near 15.1 and 15.23 μm and is less prominent in comparison; the dip-to-peak ratios, defined by Zasowski et al. (2009) as the local minimum to local maximum ratio of the blue peak, are 1.6–3.4 times less than that of HOPS-68. Second, toward these protostars a third peak or broad shoulder is often observed near 15.4 μm, but is only weakly detected in the SH spectrum of HOPS-68. Finally, the SH spectrum of HOPS-68 reveals the presence of both gaseous 14.97 μm CO$_2$ absorption and a blue absorption component or wing shortward of 15.05 μm. In comparison, gas-phase CO$_2$ absorption is weakly observed in the spectrum of the massive protostar S140 IRS 1; however, the spectrum displays no evidence for a blue wing.

3.1. Unique Component Model

We first demonstrate that the *unique component decomposition*, which generally fits the CO$_2$ bending mode profiles in

both low- and high-mass protostars, fails for HOPS-68. Following Pontoppidan et al. (2008), we use the following five components, corrected for shape effects using a continuous distribution of ellipsoids (CDE; Bohren & Huffman 1983) model: hydrogen-rich CO$_2$ (H$_2$O:CO$_2$ = 100:14; T = 10 K), CO-rich CO$_2$ (CO:CO$_2$ = 100:70, 100:26 or CO$_2$:CO = 112:100; T = 10 K), pure CO$_2$ (T = 15 K), and dilute CO$_2$ (CO:CO$_2$ = 100:4; T = 10 K). For the pure CO$_2$ component, we adopted the shape-corrected, high-resolution spectra from this work (see the Appendix). To match the resolving power of the SH module, the high-resolution spectra are convolved with a Gaussian, having an FWHM of $\Delta\lambda \approx 0.03\,\mu$m, at each wavelength element. The fifth component, often referred to in the literature as the CO$_2$ shoulder at 15.4 μm, has been identified as an intermolecular interaction between CO$_2$ and CH$_3$OH in annealed H$_2$O:CH$_3$OH:CO$_2$ mixtures (Ehrenfreund et al. 1998; Dartois et al. 1999), and is empirically modeled using a superposition of two Gaussians in the wavenumber domain.

We employ a nonlinear least-squares fitting routine (MPFIT; Markwardt 2009) to determine the best-fit scaling of each component to the observed CO$_2$ bending mode of HOPS-68:

$$\tau(\lambda) = \sum_{i=1}^{5} \alpha_i \tau_i(\lambda), \qquad (1)$$

where $\tau_i(\lambda)$ is the normalized optical depth of an individual laboratory ice component and α_i is its corresponding scaling parameter. The fit is performed over the wavelength ranges of 14.75–14.95 and 15.0–15.6 μm to avoid the gas-phase CO$_2$ absorption at 14.97 μm and the blue wing of the 16.1 μm forsterite feature.

A comparison between the best-fit model and the observed CO$_2$ bending mode of HOPS-68 is shown in the left panel of Figure 2, and clearly indicates that the ice composition is poorly simulated ($\chi_\nu^2 \approx 391$) by the unique component decomposition from Pontoppidan et al. (2008). The best-fit model results in a three-component ice mantle that is dominated by pure CO$_2$, with contributions from the CO-rich CO$_2$:CO = 112:100 mixture and the 15.4 μm shoulder component. The hydrogen-rich H$_2$O:CO$_2$ = 100:14 mixture, which generally dominates the bending mode profiles toward low- and high-mass protostars (Pontoppidan et al. 2008; Gerakines et al. 1999; Oliveira et al. 2009; Seale et al. 2011; An et al. 2011; Kim et al. 2012), is entirely absent from the model. The red wing of the observed profile is adequately matched by the pure CO$_2$ component, however the blue peak (15.14 μm) of the pure CO$_2$ spectrum does not coincide with the observed peak position of 15.05 μm. Moreover, we find that the CO-rich CO$_2$:CO = 112:100 mixture is too broad and redshifted to account for the observed blue wing of the bending mode; decreasing the CO$_2$ fraction of this mixture results in a narrow profile that becomes further redshifted.

3.2. Annealed H$_2$O:CH$_3$OH:CO$_2$ Model

We now consider the approach from Gerakines et al. (1999), who first interpreted the CO$_2$ bending mode profiles toward high-mass protostars using a combination of a hydrogen-rich mixture and an annealed CH$_3$OH-rich mixture. Similarly to Seale et al. (2011), a two-component model was assembled using the CDE shape-corrected H$_2$O:CO$_2$ = 100:14 (T = 10 K) mixture and an annealed H$_2$O:CH$_3$OH:CO$_2$ mixture from the large library of laboratory spectra described in White et al. (2009). However, since the blue peak of the observed bending mode is positioned near 15.05 μm, we consider only the bluest
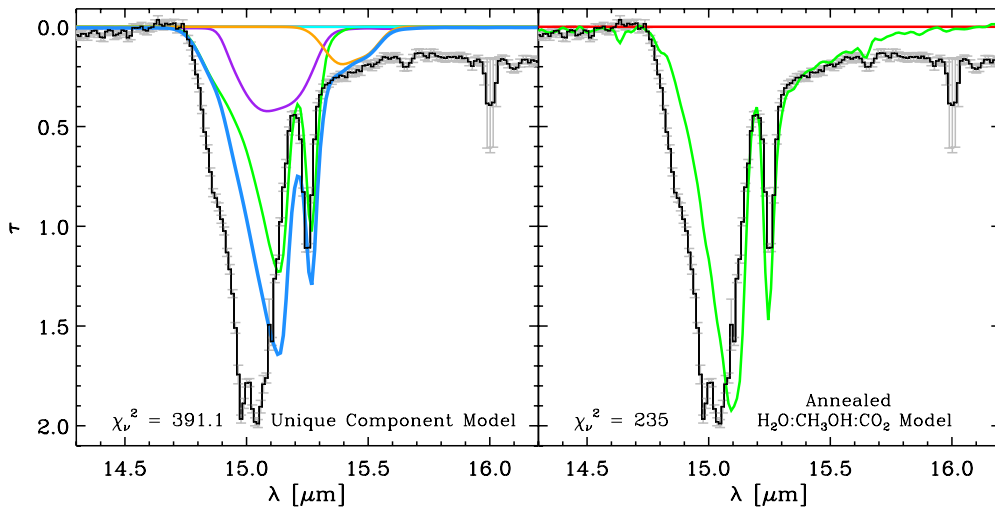
Figure 2. *Spitzer*-IRS SH optical depth spectrum of HOPS-68 (black line) and best-fit CO_2 ice models. Left panel: the best-fit unique component CDE grain shape model (blue line) from Pontoppidan et al. (2008). The model includes contributions from the pure CO_2 component ($T = 15$ K; green line), the hydrogen-poor CO_2:CO = 112:100 mixture ($T = 10$ K; violet line), and the 15.4 μm shoulder component (orange line). Right panel: the best-fit annealed ice model adopted from Gerakines et al. (1999). The model consists of the annealed H_2O:CH_3OH:CO_2 = 1:0.9:1 mixture ($T = 125$ K; green line) and the CDE shape-corrected laboratory spectrum of the hydrogen-rich H_2O:CO_2 = 100:14 mixture ($T = 10$ K; red line). The fitting procedures are constrained to wavelengths shortward of 15.6 μm to avoid the blue wing of the 16.1 μm forsterite feature.

(A color version of this figure is available in the online journal.)

($\tilde{\nu} \gtrsim 662$ cm^{-1} or $\lambda \lesssim 15.1$ μm) H_2O:CH_3OH:CO_2 spectra for simplicity. The annealed mixtures are described in Table 1. For consistency with other studies (e.g., Gerakines et al. 1999; Cook et al. 2011), grain shape corrections were not applied to the absorption spectra of annealed mixtures; the segregation of CH_3OH and CO_2 in laboratory ice mixtures is thought to result in a highly inhomogeneous structure that is no longer well represented by thin films (Gerakines et al. 1999; Ehrenfreund et al. 1999).

The best-fit model is presented in the right panel of Figure 2. In contrast to past studies (e.g., Gerakines et al. 1999; Seale et al. 2011), we find that combining the CDE shape-corrected hydrogen-rich H_2O:CO_2 = 100:14 ($T = 10$ K) mixture with an annealed H_2O:CH_3OH:CO_2 = 1:0.9:1 ($T = 125$ K) mixture yields a poor goodness of fit ($\chi_\nu^2 \approx 235$). In particular, we find that the hydrogen-rich mixture, which is known to consistently dominate the bending mode, is simply not utilized by the nonlinear least-squares fitting routine due to its broad redshifted profile. Instead, the fitting routine attempts to constrain the ice composition with a single annealed mixture. However, even for the bluest annealed mixtures, we find that the position of the blue peak does not coincide with the observed peak position of $\sim$15.05 μm. This result demonstrates that the observed CO_2 bending mode cannot be modeled by combining a hydrogen-rich mixture with an annealed H_2O:CH_3OH:CO_2 mixture, or by a single annealed H_2O:CH_3OH:CO_2 mixture. Moreover, this is consistent with the fact that the unique profile decomposition is capable of simulating the same lines of sight as the annealed ice mixtures (Pontoppidan et al. 2008).

3.3. Multi-component Homogeneous Spheres Model

Having found that the traditional methods for analyzing the CO_2 ice band profile fail for HOPS-68, we now investigate a broader set of possibilities. In particular, we must include a component that can provide additional absorption in the blue wing of the profile. To this end, we consider additional CO_2-bearing, hydrogen-poor ice analogs from Ehrenfreund et al.

(1997) and explore the effect of grain shape by using homogeneous spheres in the Rayleigh limit. The hydrogen-poor mixtures, which are summarized in Table 1, consist of two or more molecular constituents and span a laboratory temperature range of $T = 10$–80 K. Grain shape-corrected spectra for a variety of particle shape distributions are presented by Ehrenfreund et al. (1997). For relatively dilute CO_2 (e.g., H_2O:CO_2 = 100:14 and CO:CO_2 = 100:26), grain shape effects are generally weak, and only minor differences in the bending mode profile exist between the CDE and spherical grain shape corrections. Conversely, for CO_2-rich mixtures (e.g., pure CO_2 and CO_2:H_2O = 6:1), spherical grain shape corrections often result in a narrow blueshifted profile that is qualitatively consistent with the observed blue wing.

Following a similar methodology as before, a spectral decomposition of the observed bending mode was performed using the multi-component model from Pontoppidan et al. (2008). However, for this model, the choice of the hydrogen-poor CO_2 component was not restricted to the three CO-rich mixtures used by Pontoppidan et al. (2008), but instead selected from the aforementioned suite of CO_2-bearing ice analogs by Ehrenfreund et al. (1997). The laboratory temperature of the pure CO_2 component was also permitted to vary from $T = 15$–75 K. Furthermore, we assume that the line of sight consists exclusively of small homogeneous spheres.

The best-fit homogeneous spheres model is presented in the left panel of Figure 3. A four-component model, consisting largely of pure CO_2 ($T = 15$ K) and the hydrogen-poor CO_2:H_2O = 6:1 ($T = 55$ K) mixture, was found to provide the best fit ($\chi_\nu^2 \approx 19$) to the observed bending mode. As qualitatively expected, we find that the observed blue wing is adequately simulated by spherical grain shape-corrected laboratory spectra of CO_2-rich mixtures. Furthermore, the observed red wing is well matched by a combination of pure CO_2, the hydrogen-rich H_2O:CO_2 = 100:14 ($T = 10$ K) mixture, and the 15.4 μm shoulder component. However, due to the relatively low amplitude of the pure CO_2 red peak, the optical depth of the 15.24 μm peak is slightly underpredicted by the

Table 1
Summary of Laboratory Absorption Spectra

Ice Composition	Mixture Ratio	T (K)	Resolution (cm^{-1})
Hydrogen-rich ice (Ehrenfreund et al. 1997)			
$H_2O:CO_2$	100:14	10	1
Hydrogen-poor ices (Ehrenfreund et al. 1997)			
$CO:CO_2$	100:4	10	1
$CO:CO_2$	100:4	30	1
$CO:CO_2$	100:8	10	1
$CO:CO_2$	100:8	30	1
$CO:CO_2$	100:16	10	1
$CO:CO_2$	100:16	30	1
$CO:CO_2$	100:21	10	1
$CO:CO_2$	100:21	30	1
$CO:CO_2$	100:23	10	1
$CO:CO_2$	100:23	30	1
$CO:CO_2$	100:26	10	1
$CO:CO_2$	100:26	30	1
$CO:CO_2$	100:70	10	1
$CO:N_2:CO_2$	100:50:20	10	1
$CO:N_2:CO_2$	100:50:20	30	1
$CO:O_2:CO_2$	100:10:23	10	1
$CO:O_2:CO_2$	100:10:23	30	1
$CO:O_2:CO_2$	100:11:20	10	1
$CO:O_2:CO_2$	100:11:20	30	1
$CO:O_2:CO_2$	100:20:11	10	1
$CO:O_2:CO_2$	100:20:11	30	1
$CO:O_2:CO_2$	100:50:4	10	1
$CO:O_2:CO_2$	100:50:4	30	1
$CO:O_2:CO_2$	100:50:8	10	1
$CO:O_2:CO_2$	100:50:16	10	1
$CO:O_2:CO_2$	100:50:16	30	1
$CO:O_2:CO_2$	100:50:21	10	1
$CO:O_2:CO_2$	100:50:21	30	1
$CO:O_2:CO_2$	100:50:32	10	1
$CO:O_2:CO_2$	100:54:10	10	1
$CO:O_2:CO_2$	100:54:10	30	1
$CO:O_2:N_2:CO_2$	100:50:25:32	10	1
$CO:O_2:N_2:CO_2$	100:50:25:32	30	1
$CO:O_2:N_2:CO_2:H_2O$	25:25:10:13:1	10	1
$CO:O_2:N_2:CO_2:H_2O$	50:35:15:3:1	10	1
$CO:O_2:N_2:CO_2:H_2O$	50:35:15:3:1	30	1
$CO_2:CO$	112:100:1	10	1
$CO_2:CO$	112:100:1	45	1
$CO_2:H_2O$	6:1	10	1
$CO_2:H_2O$	6:1	42	1
$CO_2:H_2O$	6:1	45	1
$CO_2:H_2O$	6:1	50	1
$CO_2:H_2O$	6:1	55	1
$CO_2:H_2O$	6:1	75	1
$CO_2:H_2O$	10:1	10	1
$CO_2:H_2O$	10:1	80	1
$CO_2:H_2O$	100:1	10	1
$CO_2:H_2O$	100:1	30	1
$CO_2:O_2$	1:1	10	1
Pure CO_2 ices (this work)			
Pure CO_2	$\cdots$	15	0.1
Pure CO_2	$\cdots$	30	0.1
Pure CO_2	$\cdots$	45	0.1
Pure CO_2	$\cdots$	60	0.1
Pure CO_2	$\cdots$	75	0.1
Annealed ices (White et al. 2009)			
$H_2O:CH_3OH:CO_2$	1:0.9:1	125	1
$H_2O:CH_3OH:CO_2$	1:0.9:1	130	1
$H_2O:CH_3OH:CO_2$	1:1.7:1	110	1
$H_2O:CH_3OH:CO_2$	1:1.7:1	115	1
$H_2O:CH_3OH:CO_2$	1:1.7:1	120	1

best-fit model. Nonetheless, we conclude that an exclusive homogenous spheres model, consisting predominantly of the hydrogen-poor $CO_2:H_2O = 6:1$ ($T = 55$ K) mixture, yields an overall excellent fit to the observed CO_2 bending mode profile.

3.4. Homogeneous Spheres + CDE Model

The grain shapes of CO and CO_2 ice mantles in the circumstellar envelopes of protostars have been constrained using multiple ice bands of the same species (Boogert et al. 2002; Pontoppidan et al. 2003; Gerakines et al. 1999). A simultaneous decomposition of these bands indicates that their observed profiles are consistent with those of small irregularly shaped ice mantles, simulated by CDE grain shape models. For this reason, invoking a model consisting exclusively of homogeneous spheres may seem unjustified. However, we have demonstrated that utilizing a CDE grain shape model to simulate the CO_2 bending mode of HOPS-68 is largely unsatisfactory. Even when the choice of the hydrogen-poor component is not constrained to the CO-rich $CO:CO_2$ mixtures used by Pontoppidan et al. (2008), we find that the goodness of fit is generally poor ($\chi_\nu^2 \approx$ 90–680). Although our analysis is restricted to laboratory experiments for which grain shape corrections have been applied, this result implies that the observed blue wing is inconsistent with all available CDE shape-corrected hydrogen-poor ice analogs. In contrast, we have shown that small homogeneous spheres of the hydrogen-poor $CO_2:H_2O = 6:1$ ($T = 55$ K) ice mixture can adequately fit the blue wing of the observed bending mode.

To further examine the robustness of this result, we next consider a modeled line of sight that is populated by both spherical and irregularly shaped grains. Following a similar approach as in Section 3.3, a CO_2 ice model was constructed by combining the previously utilized CDE shape-corrected laboratory spectra (hydrogen-rich CO_2, pure CO_2, and dilute CO_2), a spherical grain shape-corrected hydrogen-poor laboratory spectrum, and the empirical 15.4 μm CO_2 shoulder component. The best-fit model is shown in the right panel of Figure 3. Indeed, we find that a four-component model, composed largely of the same homogeneous $CO_2:H_2O = 6:1$ ($T = 55$ K) spheres mixture from Section 3.3, is required for a satisfactory fit ($\chi_\nu^2 \approx 24$). The red wing of the observed bending mode is well matched by the combination of the CDE shape-corrected spectra of pure CO_2 ($T = 75$ K) and the hydrogen-rich $H_2O:CO_2 = 100:14$ ($T = 10$ K) mixture, with the 15.4 μm shoulder component. In comparison to the model results from Section 3.3, we conclude that a modeled line of sight composed of two separate grain shape populations (spherical and irregularly shaped particles) provides an equally good fit. This result demonstrates that the CO_2 bending mode profile toward HOPS-68 is largely governed by the grain shape and chemical composition of the hydrogen-poor CO_2 component.

3.5. CO_2 Ice Column Density

The column density along the line of sight for each best-fit CO_2 component was estimated from Equation (A2), adopting the pure CO_2 bending mode band strength of $A = 1.1 \times 10^{-17}$ cm molecule^{-1} from Gerakines et al. (1995). The optical depth spectra were integrated over the wavenumber range of 680.3–613.5 cm^{-1} ($\lambda = 14.7$–16.3 μm) to include the long-wavelength wing of the observed profile.

To estimate the systematic contribution from the baseline subtraction, we first computed the standard error, σ, between the best-fit continuum and the SH spectrum. The best-fit continuum
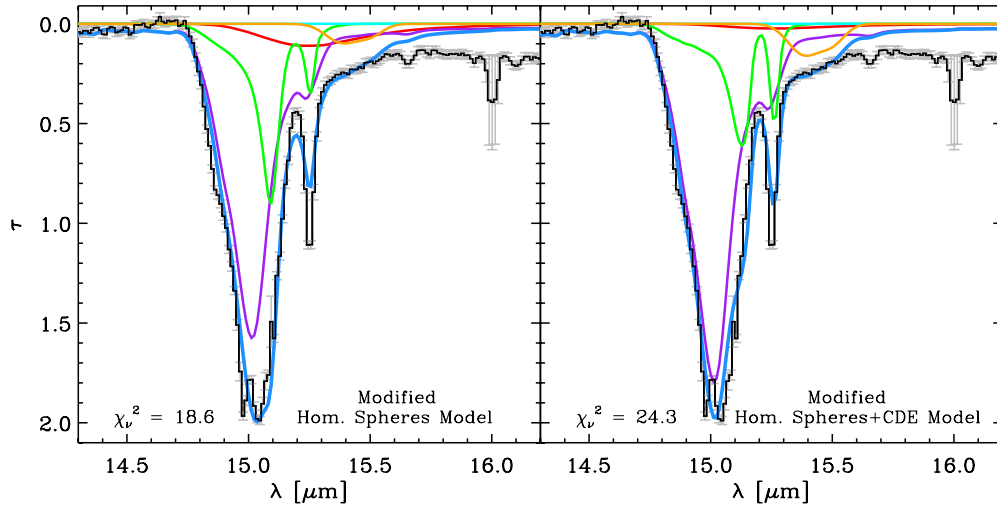
Figure 3. *Spitzer*-IRS SH optical depth spectrum of HOPS-68 (black line) and best-fit CO_2 ice models (blue lines). Left panel: the best-fit multi-component homogeneous spheres model. Individual CO_2 ice components include the hydrogen-poor CO_2 CO_2:H_2O = 6:1 mixture (T = 55 K; violet line), pure CO_2 (T = 15 K; green line), the hydrogen-rich H_2O:CO_2 = 100:14 mixture (T = 10 K; red line), and the 15.4 μm shoulder (orange line). Right panel: the best-fit multi-component CDE + spheres model. A line of sight consisting of two grain shape populations was simulated by combining the CDE shape-corrected laboratory spectra of pure CO_2 ice (T = 75 K; green line) and the hydrogen-rich H_2O:CO_2 = 100:14 mixture (T = 10 K; red line), with the homogeneous CO_2:H_2O = 6:1 spheres mixture (T = 55 K; violet line).

(A color version of this figure is available in the online journal.)

Table 2
Column Densities and Abundances for Best-fit CO_2 Ice Models

Grain Shape Model	$N(CO_2)$ (10^{17} cm^{-2})	H-rich (%)	CO-rich (%)	Pure (%)	Shoulder (%)	Dilute (%)	H-poor (%)	T_{pure} (K)	χ_ν^2
			Multi-component models						
CDE	19.83 ± 0.49	$\cdots$	27 ± 3	65 ± 3	8 ± 12	$\cdots$	$\cdots$	15	391.1
Spheres	24.66 ± 0.59	10 ± 13	$\cdots$	22 ± 3	3 ± 11	$\cdots$	65 ± 3	15	18.6
CDE + Spheres	24.53 ± 0.59	2 ± 52	$\cdots$	18 ± 3	6 ± 8	$\cdots$	74 ± 3	75	24.3
		Median abundance toward low-mass protostars (Pontoppidan et al. 2008)[a]							
CDE	$8.46^{16.20}_{4.34}$	70^{74}_{65}	20^{27}_{15}	6^{12}_{1}	3^{5}_{2}	$<0.1^{1}_{0}$	$\cdots$	15	$\cdots$

Notes. Uncertainties are based on statistical errors in the *Spitzer*-SH spectrum and systematic errors in the continuum determination. Grain shape models from this work include irregular grains (CDE), pure homogeneous spheres (spheres), and two separate grain shape populations (CDE+Spheres). For the CDE and spheres models, all CO_2 components consist of irregularly shaped particles and homogeneous spheres, respectively. For the CDE+spheres model, all components are representative of irregularly shaped particles, except for the hydrogen-poor CO_2 component, which is representative of homogeneous spheres.
[a] Median abundances include upper and lower quartile values.

was then offset by $\pm 1\sigma$ to produce new optical depth spectra and column density estimates. To quantify the errors due to the baseline uncertainty, we then calculated the mean absolute difference between the best-fit column densities and the column densities obtained by offsetting the best-fit continuum. These errors were then added in quadrature with the best-fit errors, which are returned by the least-squares minimization technique, to generate the final CO_2 ice column density uncertainties.

The column densities and relative abundances for the best-fit CO_2 ice models are tabulated in Table 2. The modified spectral decomposition analysis gives us the following three observables: (1) among the available laboratory ice analogs, homogeneous spheres of the hydrogen-poor CO_2:H_2O = 6:1 (T = 55 K) mixture are required to match the blue wing of the observed CO_2 bending mode. This component constitutes 65%–74% of the total CO_2 ice column density along the line of sight. (2) The red wing of the observed profile can be modeled by combining pure CO_2 ice and the 15.4 μm CO_2 shoulder component. The pure CO_2 component constitutes 18%–22% of the total CO_2 ice column density, while only a minor (3%–6%) contribution

is attributed to the 15.4 μm CO_2 shoulder component. (3) Only 2%–10% of the total CO_2 ice column density is composed of the hydrogen-rich component, while no evidence for the CO-rich component is found within the observed CO_2 bending mode. These fundamental differences of HOPS-68, as compared to the typical ice structure toward low-mass protostars, are illustrated in Table 2.

To derive the CO_2 ice abundance, the H_2O ice column density toward HOPS-68 was estimated from the 12 μm libration mode of the amorphous silicate-subtracted optical depth spectrum from Poteet et al. (2011). Adopting an intrinsic band strength of $A = 2.9 \times 10^{-17}$ cm molecule^{-1} for crystalline H_2O ice (T = 140 K; Mastrapa et al. 2009), we calculate an H_2O ice column density of $N(H_2O) = (88.2 \pm 0.7) \times 10^{17}$ cm^{-2}. For the best-fit models from Sections 3.3 and 3.4, we calculate an average CO_2-to-H_2O ice column density ratio of $N(CO_2)/N(H_2O) = 0.28 \pm 0.03$. This is consistent with abundances measured toward low-mass protostars ($N(CO_2)/N(H_2O) = 0.32 \pm 0.02$; Pontoppidan et al. 2008), but is significantly greater than those observed for high-mass

protostars ($N(CO_2)/N(H_2O) = 0.17 \pm 0.03$; Gerakines et al. 1999).

4. DISCUSSION AND CONCLUSIONS

4.1. The Rarity of Highly Processed Ice

The *Spitzer*-IRS SH spectrum toward the low-mass protostar HOPS-68 reveals a rare 15.2 μm CO_2 bending mode profile, exhibiting a prominent double-peaked substructure (near 15.05 and 15.24 μm) and a strong blue absorption wing. Our analysis demonstrates that the observed bending mode cannot be modeled using the unique component models from Pontoppidan et al. (2008) or by combining a hydrogen-rich mixture with an annealed $H_2O:CH_3OH:CO_2$ mixture (Gerakines et al. 1999). However, when the Pontoppidan et al. (2008) models are modified to include spherical grains and a broader selection of hydrogen-poor ice mixtures, an overall excellent fit to the observed CO_2 bending mode is obtained.

Our results indicate that most (87%–92%) of the CO_2 along the line of sight is present in ices where CO_2 is the dominant constituent. In contrast, the majority of the CO_2 ice observed toward most low- and high-mass protostars is found in environments dominated by H_2O and CO. For example, toward low-mass protostars, Pontoppidan et al. (2008) showed that generally ∼70% of the total CO_2 ice column density is composed of the hydrogen-rich component, while ∼20% is attributed to the CO-rich component. Furthermore, the median abundance of pure CO_2 ice to the total CO_2 ice column density is found to be ∼6%.

The nearly complete lack of unprocessed ice mantles along the line of sight toward HOPS-68 is unexpected. For example, toward the prominent low-mass sources IRAS 03254 and RNO 91, comparable fractions of pure CO_2 (17%–23%) are reported by Pontoppidan et al. (2008). However, a substantial fraction (70%–75%) of their total CO_2 ice column density is attributed to unprocessed ice mixtures (CO:CO_2 and $H_2O:CO_2$), which lie outside the distillation and segregation radii (Öberg et al. 2011). In this context, the ice mantles toward HOPS-68 are uniquely different from those observed toward other protostars, indicating that the observed icy grains have undergone a higher degree of thermal processing.

4.2. The Origin of Processed Ice toward HOPS-68

Nearly 100 CO_2 ice spectra have been described in the literature, and the observed profile toward HOPS-68 is unique among them. It is therefore unlikely to find more than a few percent of HOPS-68 ice analogs in a larger sample of protostars. Is this rarity due to HOPS-68 being fundamentally different than other protostars, or does the observed line of sight reveal processed ices that are present in other protostars, but which are typically obscured by their cold outer envelope?

4.2.1. The Lack of Unprocessed Ice

A peculiar spectral property of HOPS-68 is the combination of a relatively flat 8–70 μm SED and strong silicate absorption at 9.7 μm (Poteet et al. 2011, Figure 3). To reproduce these observed characteristics, Poteet et al. (2011) employed a radiative transfer model based on the collapse of an isothermal sheet initially in hydrostatic equilibrium (Hartmann et al. 1994, 1996). They conclude that HOPS-68 possesses a highly flattened ($\eta = 2.0$) protostellar envelope, as described by the degree of asphericity ($\eta = R_{\max}/H$, where $R_{\max}$ is the outer envelope radius

and H is the scale height of the initial sheet). In comparison, Furlan et al. (2008) found that most Taurus protostars do not require an initially flattened density distribution, but instead can be modeled by the collapse of an initially spherically symmetric cloud core (Terebey et al. 1984). Unlike spherical envelopes, an implication of the highly flattened structure is that cold material in the outer envelope is not expected to be present along the observed line of sight. Indeed, we estimate that ≲15% of the gas has temperatures below $T = 30$ K. Thus, the absence of the volatile CO-rich CO_2 component and the low abundance of the hydrogen-poor CO_2 component may be explained by the lack of cold, unprocessed dust along the line of sight. This result suggests that highly processed ices may be present in the inner regions of other protostellar envelopes, but are likely obscured or diluted by the large, cold envelopes of unprocessed material typically surrounding them.

Furthermore, to simultaneously simulate the strong silicate absorption, the Poteet et al. (2011) model requires infalling material to be deposited within 0.5 AU of the central protostar, as set by the centrifugal radius (R_c). In contrast, R_c values from 10 to 300 AU, with a median of 60 AU, were found for Taurus protostars (Furlan et al. 2008). For a centrifugal radius of $R_c = 0.5$ AU, we estimate that more than 50% of the infalling material along the line of sight is concentrated within 10 AU of the central protostar, where the potential for thermal processing of icy grains by radiation and outflow-induced shocks is the strongest.

Resolved images of protostellar envelopes show a wide range of envelope morphologies, from highly flattened to relative spheroidal structures, as well as a great deal of complexity (Tobin et al. 2010, 2011, 2012). The diversity of envelope morphologies may be due to formation of protostars in turbulent and often filamentary molecular clouds (e.g., André et al. 2010; Molinari et al. 2010). Although the envelope of HOPS-68 has not yet been resolved, SED modeling requires a highly flattened envelope, which may be uncommon within the diversity of envelope morphologies typically found in molecular clouds. This flattened envelope, when observed from an intermediate inclination, results in a line of sight that is less obscured by unprocessed material in the cold, outer envelope.

4.2.2. The Formation of Spherical CO_2-rich Mantles

Although a flattened envelope structure may explain the absence of cold primordial ices seen toward other protostars, it does not directly explain why a large fraction of the CO_2 ice seen toward HOPS-68 is sequestered as spherical, CO_2-rich mantles, while typical interstellar ices show evidence of irregularly shaped, hydrogen-rich mantles. That is, in the absence of unprocessed ices along the line of sight, the observed CO_2 ice profile should be consistent with irregularly shaped CO_2-rich ice mantles. Irregularly shaped ice mantles are generally understood to be the product of a slow aggregation of icy grain monomers in dense molecular clouds prior to protostellar collapse (Ossenkopf 1993; Ormel et al. 2009). In the case of HOPS-68, we propose that the spherical ice mantles may have formed as the volatiles rapidly freeze out in dense gas, following an energetic but transient event that sublimated any primordial icy grain population within its inner envelope region.

Radiative processing by episodic accretion events has recently been proposed by Kim et al. (2012) to be a viable mechanism for producing pure CO_2 ice, through the distillation process, toward low-luminosity protostars ($L \lesssim 1\,L_\odot$). Using the unique component decomposition from Pontoppidan et al. (2008), Kim

et al. (2012) report a median pure CO_2 ice abundance of 15% toward six protostars; this value is six times less than the processed ice abundance found toward HOPS-68. The detection of pure CO_2 ice toward low-luminosity protostars indicates that a transient phase of higher luminosity must have existed some time in their past (Kim et al. 2012). For the case of HOPS-68, we propose that heating beyond the sublimation temperature of H_2O ice ($T \approx 110$ K; Fraser et al. 2001) will evaporate ice mantles close to the central protostar during the high-luminosity phase, resulting in the separation of icy grain conglomerates. As the protostar later returns to its quiescent, low-luminosity phase, gas temperatures in the envelope decrease and H_2O and CO_2 rapidly ($t < 10^3$ yr) condense onto grain surfaces in the order of their condensation temperature (Ossenkopf 1993), provided that the gas is sufficiently dense ($n_{H_2} > 10^4$ cm^{-3}). This mechanism naturally allows for the formation of nearly pure CO_2 ice mantles sequestered on spherical grains. However, this scenario requires that the accretion outburst must have occurred recently to avoid the reproduction of irregular grains by renewed grain aggregation.

Evidence for transient heating is often presumed from the variable nature of the accretion luminosity. Photometric monitoring of HOPS-68, with the *Herschel Space Observatory*, reveals a ~21% variation in the 70 μm flux over a two-week period; this variability is most likely driven by variations in the mass accretion rate onto the central protostar (Billot et al. 2012). While larger increases in luminosity, over longer timescales, are certainly needed to heat dust grains to the sublimation temperature of H_2O ice, the observed variability indicates a rapidly changing accretion rate for HOPS-68, and hence, supports the possibility of a recent ($t \ll 10^6$ yr) accretion outburst that raised the luminosity significantly above the current observed value.

In order to quantify the luminosity rise needed to produce the proposed sublimation of icy grains, we increase the total luminosity of the Poteet et al. (2011) SED model by a factor of 10, 50, and 100. Adopting a CO_2 ice desorption temperature of $T = 45$ K, from an amorphous H_2O ice surface (Noble et al. 2012), we assume that CO_2 ice is present in the envelope of HOPS-68 at distances greater than $r \approx 90$ AU. These incremental steps in luminosity result in increased dust temperatures of $T = 70$, 97, and 113 K at $r \approx 90$ AU, respectively. Thus, for HOPS-68, we propose that a factor of 100 increase in luminosity (~100 $L_\odot$) is required to thermally desorb CO_2 and H_2O ices from the surface of dust grains. Although the required luminosity is higher than the typical luminosities of protostars in Orion (~1 $L_\odot$; Kryukova et al. 2012), luminosities in excess of 100 $L_\odot$ are observed toward young, low-mass stars undergoing FU Orionis-like outbursts (Reipurth & Aspin 2010). Kryukova et al. (2012) find five Orion protostars with luminosities exceeding 100 $L_\odot$, including two candidate FU Orionis-like objects. Furthermore, models developed to explain the typical low luminosities of protostars require that most low-mass protostars undergo FU Orionis-like outbursts in order to accrete the required amount of mass during the protostellar lifetime (Dunham & Vorobyov 2012).

Alternatively, mechanical processing by shocks, associated with the observed outflow (Williams et al. 2003), will also sublimate ice mantles in the outflow working surface along the cavity wall. In dense shocks, dust grain temperatures are raised by collisional heating with hot gas particles and by absorption of photons as the compressed gas cools, resulting in thermal desorption and sputtering of interstellar ices. In particular, for a nondissociative shock with a velocity of $v_s = 10$ km s^{-1},

dust grains are expected to be heated to temperatures on the order of 10^2 K (Neufeld & Hollenbach 1994), which is more than sufficient to allow for a condensation sequence to occur behind the shock. Therefore, we propose that nearly pure CO_2 ice mantles are formed in post-shocked gas, in a condensation sequence similar to that proposed for the accretion outburst scenario, and that the line of sight must be dominated by shock-processed material near the cavity wall. For other orientations, the line of sight will be dominated by irregularly shaped icy grain mantles. Toward HOPS-68, evidence for the presence of shock-processing may be inferred from the detection of [S I], [Fe II], and [Si II] forbidden emission at 25.25, 25.98, and 34.82 μm, respectively (D. M. Watson et al., in preparation), as well as gaseous absorption from C_2H_2, HCN, and CO_2 at 13.71, 14.05, and 14.97 μm, respectively.

We note that the formation of interstellar ices in a post-shocked gas was originally proposed by Bergin et al. (1998, 1999). However, in their scenario, CO_2 ice is formed by virtue of gas-phase reactions (CO + OH $\rightarrow$ CO_2 + H) and subsequent freezeout. The formation process is largely governed by the photodissociation rate of H_2O molecules by cosmic-ray-induced photons, and is expected to occur over a timescale of $t \approx 10^5$ yr at the assumed density of $n_{H_2} = 10^5$ cm^{-3}; however, the timescale may be shortened with higher gas densities or larger cosmic-ray ionization rates. Nonetheless, this long timescale for CO_2 ice mantle formation would allow for the re-development of irregularly shaped grains, through the aggregation of small regular particles. In contrast, the detection of spherical icy grains implies that ice mantle formation would have occurred more recently, over much shorter timescales ($t \sim \mathcal{O}(10^2)$ yr) and at higher densities ($n_{H_2} \approx 10^7$ cm^{-3} at $r = 100$ AU), by evaporation and re-condensation processes alone.

In summary, we propose that the observed 15.2 μm CO_2 ice profile may result from the combination of two circumstances. First, the nearly complete absence of unprocessed ices along the line of sight is due to the highly flattened envelope of HOPS-68, which lacks cold absorbing material in its outer envelope, and possesses a large fraction of material within its inner (10 AU) envelope region. Second, an energetic event led to the evaporation of inner envelope ices, followed by cooling and re-condensation, explaining the sequestration of CO_2 in a hydrogen-poor mixture and the spherical shape of the icy grains. Regardless of which energetic process is responsible for producing the spherical mantles, we note that both proposed mechanisms require fortuitous timing and orientations, and hence are consistent with the observed rarity of spherical icy grains toward protostars.

The notion of ices forming in a cooling gas, following an energetic event, makes several predictions. Water ice condensed at high temperatures will arrange itself into a crystalline matrix, predicting that the H_2O ice seen toward HOPS-68 should be predominantly crystalline. Evidence for the presence of crystalline H_2O ice was predicted, by Poteet et al. (2011), from the 12 μm libration mode. This prediction can be further tested by observing the profile of the 3.08 μm H_2O stretching mode. Carbon monoxide ice, observed at 4.67 μm, should either be absent if the temperature of the absorbing material is still above 20 K, or should show evidence of spherical grain shapes, in sharp contrast to that observed toward typical protostars (Pontoppidan et al. 2003). Finally, the $^{12}CO_2$ and $^{13}CO_2$ stretching modes at 4.27 and 4.38 μm, respectively, should be consistent with spherical grains and a nearly pure CO_2 mixture. Using the best-fit models from Sections 3.3 and 3.4, predictions for the
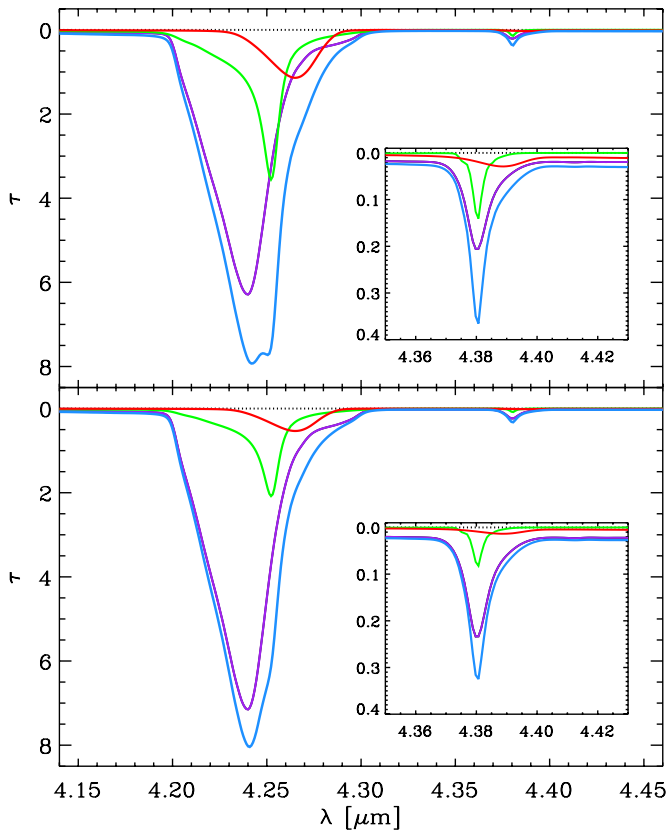
Figure 4. Model predictions for the $^{12}CO_2$ ($\tilde{v}_3$) and $^{13}CO_2$ ($\tilde{v}_3$) stretching modes at 4.27 and 4.38 μm, respectively. The predicted CO_2 profiles (blue lines) are constructed from the best-fit multi-component homogeneous spheres model (Section 3.3; top panel) and the multi-component CDE + homogeneous spheres model (Section 3.4; bottom panel). The individual ice components include: hydrogen-rich CO_2 (H_2O:CO_2 = 100:14 at T = 10 K; red lines), hydrogen-poor CO_2 (CO_2:H_2O = 6:1 at T = 55 K; violet lines), and pure CO_2 (T = 15 and 75 K; green lines).

(A color version of this figure is available in the online journal.)

$^{12}CO_2$ and $^{13}CO_2$ stretching modes are presented in Figure 4. While HOPS-68 is too faint at 3–5 μm for current spectrometers, these tests will likely be within reach of the *James Webb Space Telescope*.

This work is based on observations made with the *Spitzer Space Telescope*, which is operated by the Jet Propulsion Laboratory (JPL), California Institute of Technology (Caltech), under a contract with NASA. Support for this work was provided by NASA through contracts 1289605 and 1355568 issued by JPL/Caltech. This publication makes extensive use of data products from the Sackler Laboratory for Astrophysics at Leiden University and the Astrophysics Laboratory at the University of Alabama at Birmingham. C.A.P thanks Karin Öberg for suggesting the laboratory experiments, and Pascale Ehrenfreund, Perry Gerakines, and Adwin Boogert for insightful discussions.

APPENDIX

PURE CO_2 ICE LABORATORY SPECTRA

The infrared absorption bands of CO_2 have been extensively studied in the laboratory by Hudgins et al. (1993), Ehrenfreund et al. (1997), and Baratta & Palumbo (1998). Collectively, these studies present absorption spectra and optical constants for pure

CO_2 at laboratory temperatures of T = 10, 12, 30, 50, 70, and 80 K. These experiments are conducted under high-vacuum (HV) conditions at a spectral resolution of 1–2 cm^{-1}, too low to fully resolve the narrow structure of the Davydov split. More recently, CO_2 experiments with a spectral resolution of 0.5 cm^{-1} have been conducted at laboratory temperatures of T = 15–90 K (van Broekhuizen et al. 2006), but at a relatively low signal-to-noise ratio.

In this paper, we deploy new high-quality infrared absorption spectra and optical constants from a temperature-series laboratory study of pure, crystalline CO_2 ice. The experiments were conducted at an improved spectral resolution of 0.1 cm^{-1} and at a higher signal-to-noise ratio with respect to previous laboratory studies.

A.1. Experimental Procedure

Following the procedures of Gerakines et al. (1995) and Bouwman et al. (2007), the experiments are performed in an HV chamber with a base pressure of $P \approx 5 \times 10^{-7}$ mbar at room temperature. The chamber houses a CsI (cesium iodide) substrate that is cooled down to 15 K by a closed cycle helium cryostat (ADP DE-202). The substrate temperature is controlled with a resistive heater element and a silicon diode sensor using an external control unit (LakeShore 330).

A sample of CO_2 (Praxair, 99.998% purity) is introduced into the system from a gas bulb at 10.0 mbar prepared in a separate vacuum manifold (base pressure of $P \approx 10^{-5}$ mbar). Pure CO_2 ices are grown onto the substrate at 15 K via effusive dosing along the surface normal at a deposition rate of $\sim 10^{15}$ molecules cm^{-2} s^{-1}. The ices are heated to temperatures of T = 15, 30, 45, 60, and 75 K at a rate of 2 K minute^{-1} and allowed to relax at each temperature for five minutes before recording the absorption spectra. A Fourier Transform Infrared spectrometer (Varian 670-IR) is used to record the ice spectra in transmission mode over the wavenumber range of $\tilde{v}$ = 4000–400 cm^{-1} (λ = 2.5–25 μm) with a spectral resolution of 0.1 cm^{-1}, averaging a total of 256 scans to increase the signal-to-noise ratio. Background spectra are acquired at 15 K prior to deposition and subtracted from the recorded ice spectra.

A.2. Experimental Results

To facilitate a comparison with astronomical spectra, a baseline correction is applied to all laboratory absorption spectra by fitting a third-order polynomial over the wavenumber regions of 4000–3800, 2900–2700, 2270–2250, 950–700, and 645–640 cm^{-1}. The background- and baseline-corrected absorption spectra for pure CO_2 ice are shown in Figure 5 for the $^{12}CO_2$ ($\tilde{v}_3$) and $^{13}CO_2$ ($\tilde{v}_3$) stretching and CO_2 ($\tilde{v}_2$) bending vibrational modes.

The spectra do not suffer from any significant contamination by background gases of H_2O within the vacuum system. However, weak traces of gaseous CO_2, near 668 cm^{-1} (λ = 14.97 μm), are present in some absorption spectra, and are the result from either an under- or oversubtraction of background CO_2 gas. To reduce the noise and eliminate the gas-phase CO_2 absorption, a nonlinear least-squares minimization is simultaneously performed to the $^{12}CO_2$ $\tilde{v}_3$, $^{13}CO_2$ $\tilde{v}_3$, and CO_2 $\tilde{v}_2$ vibrational modes using a superposition of Gaussians. Figure 6 illustrates the "smoothing" technique for the CO_2 bending mode spectrum at T = 45 K. The measured peak positions ($\tilde{v}$) and widths (FWHM; $\Delta\tilde{v}$) of the CO_2 bending mode are listed in Table 3. The position of the absorption peaks near 654.5 and
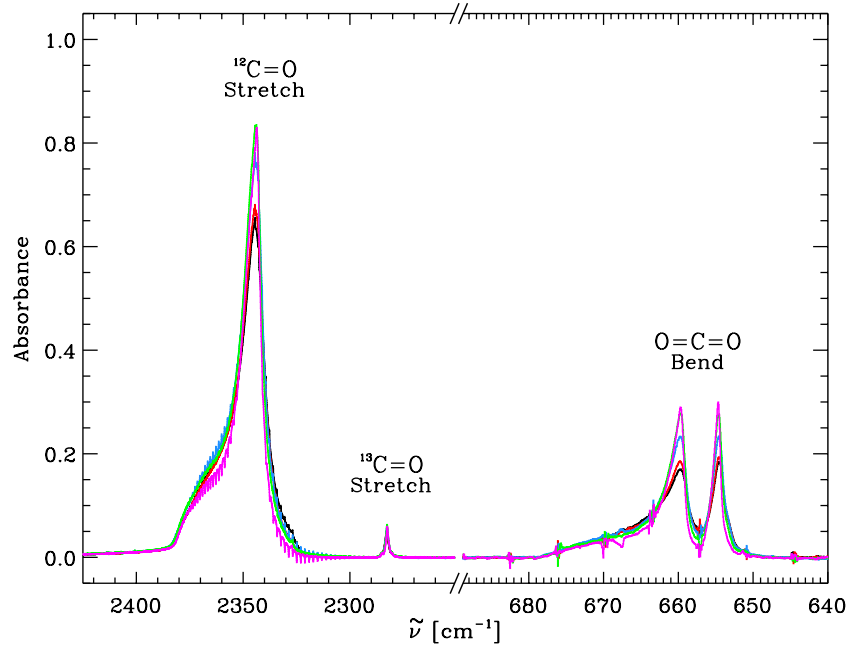
Figure 5. Background- and baseline-corrected absorption spectra of pure CO_2 ice. The $^{12}CO_2$ ($\tilde{\nu}_3$) and $^{13}CO_2$ ($\tilde{\nu}_3$) stretching (2343 and 2283 cm^{-1}, respectively) and $^{12}CO_2$ ($\tilde{\nu}_2$) bending (660 and 655 cm^{-1}) modes are shown at laboratory temperatures of $T = 15$ (black line), 30 (red line), 45 (blue line), 60 (green line), and 75 K (magenta line). Gas-phase CO_2 at 668 cm^{-1} is a background-subtraction artifact, arising from either under- or oversubtraction of background CO_2 gas.
(A color version of this figure is available in the online journal.)

Table 3
Band Positions and FWHMs of the CO_2 Bending Mode

T	$\tilde{\nu}$	FWHM, $\Delta\tilde{\nu}$	Ice Thickness, d	
(K)	(cm^{-1})	(cm^{-1})	(ML)[a]	(μm)
		Laboratory spectrum		
15	654.5/659.7	2.1/5.3	366	0.203
30	654.5/659.8	2.0/4.3	367	0.203
45	654.5/659.7	1.8/3.6	410	0.227
60	654.6/659.7	1.5/2.9	405	0.224
75	654.7/659.7	1.1/2.3	355	0.197
		CDE model		
15	654.9/660.6	2.1/7.7	$\cdots$	$\cdots$
30	655.0/660.7	2.1/6.6	$\cdots$	$\cdots$
45	655.0/660.7	1.9/5.3	$\cdots$	$\cdots$
60	655.1/661.0	1.7/4.6	$\cdots$	$\cdots$
75	655.3/661.0	1.6/4.3	$\cdots$	$\cdots$
		Homogeneous spheres model		
15	655.6/662.6	1.4/3.6	$\cdots$	$\cdots$
30	655.6/662.5	1.3/2.4	$\cdots$	$\cdots$
45	655.6/662.4	1.1/0.9	$\cdots$	$\cdots$
60	655.6/662.3	0.9/0.5	$\cdots$	$\cdots$
75	655.8/662.4	0.6/0.3	$\cdots$	$\cdots$
		Ice-coated spheres model[b]		
15	655.0/660.4/666.4	2.0/13.7	$\cdots$	$\cdots$
30	655.0/660.4/665.8	1.9/12.8	$\cdots$	$\cdots$
45	655.0/660.4/664.8	1.7/9.6	$\cdots$	$\cdots$
60	655.1/660.5/664.4	1.4/6.3	$\cdots$	$\cdots$
75	655.2/660.6/664.4	0.7/4.8	$\cdots$	$\cdots$

Notes. The band position and FWHM are listed for the multiple peaks within the CO_2 bending mode.
[a] 1 monolayer (ML) $\approx 10^{15}$ molecules cm^{-2}.
[b] For broad profiles exhibiting blended peaks, the FWHM value represents the overall width of the profile containing multiple peaks.
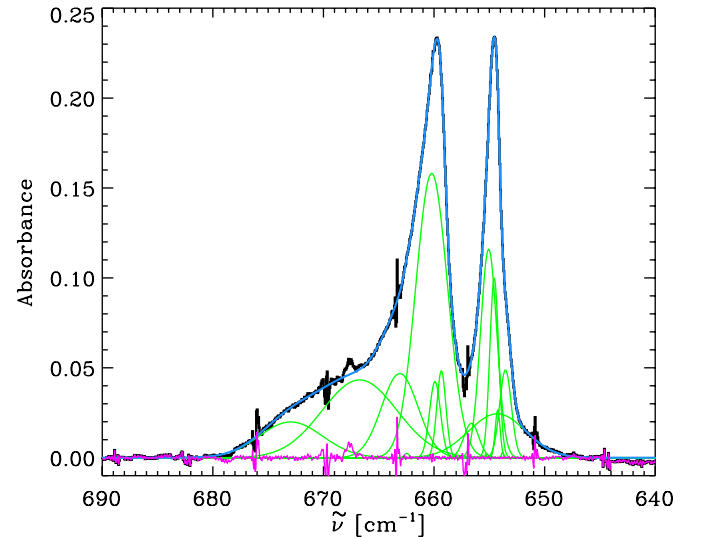

Figure 6. Laboratory bending mode ($\tilde{\nu}_2$) spectrum of pure CO_2 ice (black line) compared to its corresponding "smoothed" spectrum (blue line) at $T = 45$ K. A least-squares fit is performed using a superposition of Gaussians (green lines) to eliminate noise and gas-phase CO_2 absorption at 668 cm^{-1}. The resultant fit residuals (magenta line) are shown for comparison.
(A color version of this figure is available in the online journal.)

659.7 cm^{-1} are temperature independent and remain constant to within 0.1 cm^{-1}, while their FWHMs decrease by a factor of two with increasing temperature from $T = 15$ to 75 K. These results are in agreement with the 0.5 cm^{-1} resolution study by van Broekhuizen et al. (2006).

A.3. Optical Constants

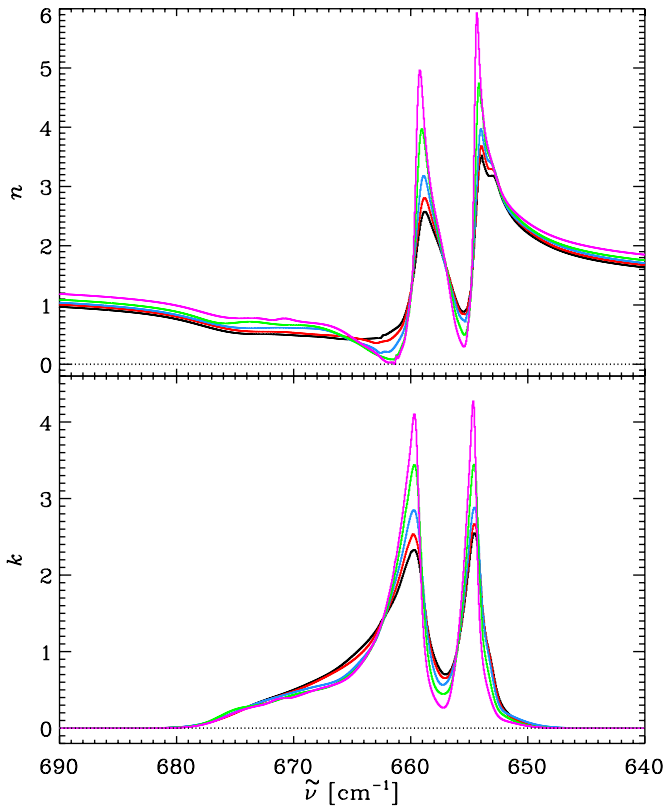The complex index of refraction ($n + ik$) is determined using a Kramers–Kronig analysis, following similar methods

Figure 7. Optical constants (n and k) for the bending mode ($\tilde{\nu}_2$) of pure CO_2 ice at laboratory temperatures of $T = 15$ (black line), 30 (red line), 45 (blue line), 60 (green line), and 75 K (magenta line).

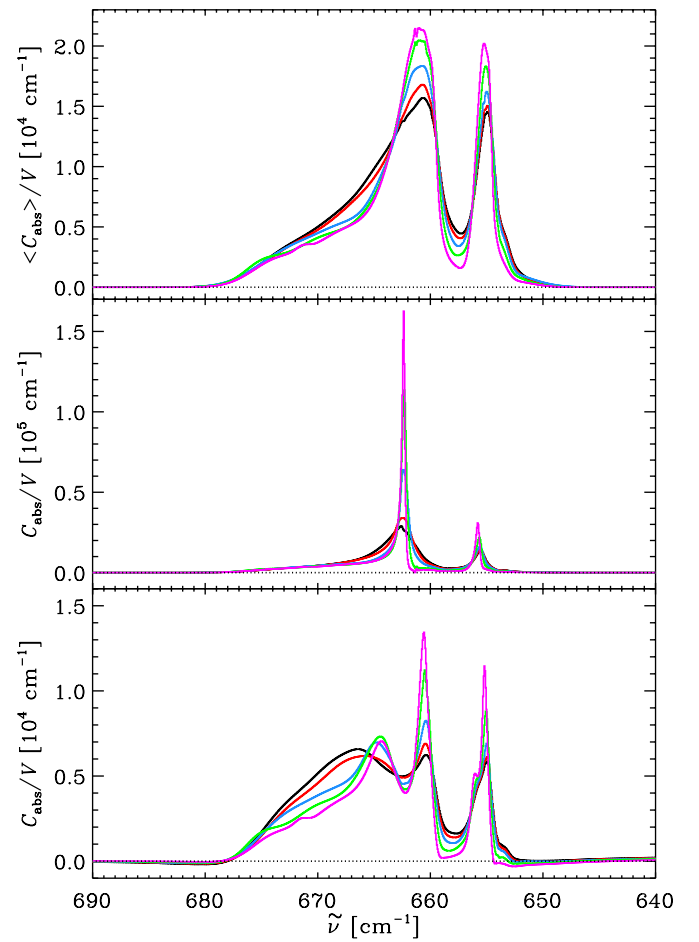(A color version of this figure is available in the online journal.)

Figure 8. Absorption cross section per unit volume for the bending mode ($\tilde{\nu}_2$) of pure CO_2 ice. Grain shape models in the Rayleigh limit are shown for a continuous distribution of ellipsoids (CDE; top panel), homogeneous spheres (middle panel), and ice-coated silicate spheres (bottom panel) at laboratory temperatures of $T = 15$ (black line), 30 (red line), 45 (blue line), 60 (green line), and 75 K (magenta line).

(A color version of this figure is available in the online journal.)

previously described in Hudgins et al. (1993) and Mastrapa et al. (2009).

Briefly, the imaginary part of the complex refractive index, k, is calculated from the Beer–Lambert law:

$$\alpha(\tilde{\nu}) \equiv 4\pi k \tilde{\nu} = \frac{1}{d} \ln(10) A_{\tilde{\nu}}, \qquad (A1)$$

where α is the Lambert absorption coefficient, d is the thickness of the ice, and $A_{\tilde{\nu}}$ is the absorbance of the ice at wavenumber $\tilde{\nu}$. The thickness of the ice samples was estimated using the known absorption band strength of pure CO_2 ice. In this technique, the column density, N (in molecules cm^{-2}), of the sample was determined using

$$N = \frac{\int \tau_{\tilde{\nu}} \, d\tilde{\nu}}{A}, \qquad (A2)$$

where $\tau_{\tilde{\nu}} = \ln(10) A_{\tilde{\nu}}$ is the optical depth and A is the intrinsic band strength of the CO_2 bending mode as determined from previous laboratory studies ($A = 1.1 \times 10^{-17}$ cm molecule^{-1}; Gerakines et al. 1995). The ice thickness is then inferred from the derived column density assuming a monolayer (ML) surface coverage of $\sim 10^{15}$ molecules cm^{-2}. The final ice thickness is tabulated in Table 3 and ranges in value from 355 to 410 ML. Assuming a monolayer thickness of 5.54 Å, the lattice constant for solid CO_2 (Keesom & Köhler 1934), these values correspond to a physical thickness of ~ 0.20–0.23 μm.

Given the absorption coefficient, the real part of the complex refractive index, n, is then calculated from the Kramers–Kronig dispersion relationship:

$$n(\tilde{\nu}) = n_0 + \frac{1}{2\pi^2} \mathscr{P} \int_{400}^{4000} \frac{\alpha(\tilde{\nu}')}{\tilde{\nu}'^2 - \tilde{\nu}^2} \, d\tilde{\nu}', \qquad (A3)$$

where $\mathscr{P}$ denotes the Cauchy principal value of the integral and n_0 is the refractive index for the high-wavenumber end of the infrared spectrum ($\tilde{\nu} > 4000$ cm^{-1}). Because the visible ($\lambda = 0.633$ μm) refractive index of pure CO_2 ice is temperature dependent, we adopt values of $n_0 \approx 1.23$, 1.26, 1.29, and 1.34 for the laboratory temperatures of $T = 15$, 30, 45, and 60 K, respectively (Satorre et al. 2008). For the absorption spectrum at $T = 75$ K, we use a value of $n_0 \approx 1.44$ from Seiber et al. (1971) to ensure that n is positive for all wavenumbers. Optical constants for the bending mode ($\tilde{\nu}_2$) of pure CO_2 are presented in Figure 7.

While our study is not intended to address the differences between the CO_2 optical constants derived in this work and those found among the literature, we do note, however, that any discrepancies are most likely due to differences in ice sample thickness and the n_0 refractive index for the high-wavenumber region ($\tilde{\nu} > 4000$ cm^{-1}). For a thorough discussion on the discrepancies between CO_2 optical constants derived
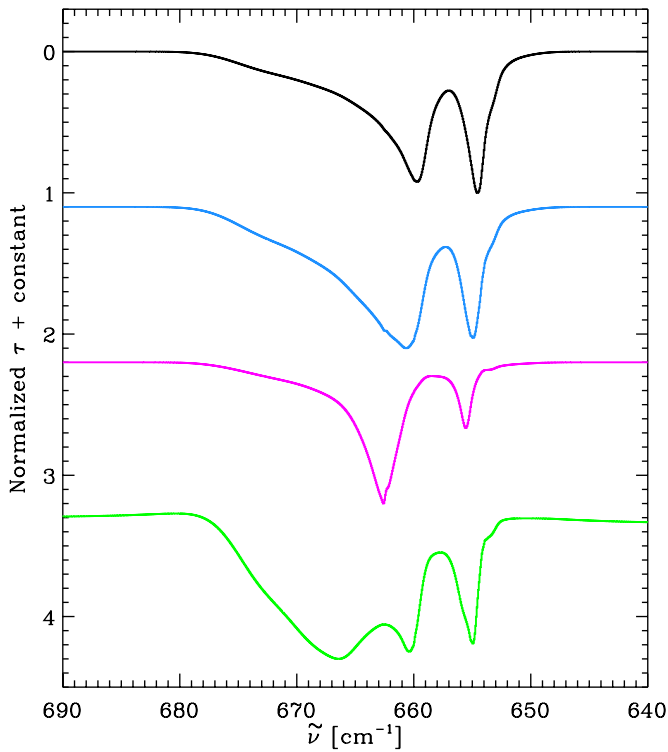
Figure 9. Normalized optical depth profiles for the bending mode ($\tilde{\nu}_2$) of pure CO_2 ice. The uncorrected laboratory spectrum at $T = 15$ K (black line) is compared to three standard grain shape models in the Rayleigh limit: a continuous distribution of ellipsoids (CDE; blue line), homogeneous spheres (magenta line), and ice-coated amorphous silicate spheres (green line).

(A color version of this figure is available in the online journal.)

from different studies, we refer the reader to Ehrenfreund et al. (1997).

A.4. Grain Size and Shape Corrections

The profiles of strong infrared resonance features, including those of ices, depend significantly on the shape and size of the absorbing and scattering particles (Tielens 1991; Dartois 2006). For pure CO_2 ice, grain size and shape corrections must be applied to the laboratory absorption spectra of thin films to allow for an accurate comparison to astronomical spectra. While irregularly shaped grain models have been largely successful at simulating astronomical spectra of CO and CO_2 ices (Pontoppidan et al. 2003; Gerakines et al. 1999), we also consider here the shape effects of spherical grain models.

Using the derived optical constants of pure CO_2, standard formulae from Bohren & Huffman (1983) were applied in the Rayleigh limit to calculate the absorption cross section per unit volume, C_{abs}/V, for a CDE (all shapes are equally probable), homogeneous spheres, and ice-coated amorphous silicate spheres. For the ice-coated spheres model, we adopt amorphous silicate optical constants from Draine & Lee (1984) and assume that half of the total particle volume is occupied by the core. Note, however, for thick ice mantles or silicate cores that occupy $\lesssim 10\%$ of the total particle volume, the ice-coated spheres profile approximates that of pure homogeneous spheres.

The absorption cross sections for the bending mode of CO_2 are presented in Figure 8 for the different grain shape models. The CDE model produces a broad double-peaked absorption profile that remains mostly constant with increasing temperature from $T = 15$ to 75 K; the peak positions exhibit a blueshift

of 0.4 cm^{-1} at $T = 75$ K. Conversely, a narrow double-peaked structure is generated by the homogenous spheres model, whose FWHMs become narrower with increasing temperature; the FWHM of the 662.5 cm^{-1} peak decreases by a factor of 12 from $T = 15$ to 75 K. In agreement with Ehrenfreund et al. (1997), we find that the ice-coated silicate spheres model gives rise to a broad triple-peaked profile.

A comparison between the different grain shape models and the laboratory spectrum of pure CO_2 at $T = 15$ K is presented in Figure 9. For all models, the peak positions and FWHMs deviate from those of the original laboratory spectrum. For the CDE model, we find that the profile becomes blueshifted and broadened by ~ 1 and ~ 2.5 cm^{-1}, respectively. For the homogeneous spheres model, a large blueshift of ~ 3 cm^{-1} and a narrowing of ~ 2 cm^{-1} are observed compared to the laboratory spectrum. For a full comparison of the spectra, the reader is referred to Table 3.

REFERENCES

An, D., Ramrez, S. V., Sellgren, K., et al. 2011, ApJ, 736, 133
André, P., Menshchikov, A., Bontemps, S., et al. 2010, A&A, 518, L102
Arce, H. G., Shepherd, D., Gueth, F., et al. 2007, in Protostars and Planets V, Vol. 951, ed. B. Reipurth, D. Jewitt, & K. Keil (Tucson, AZ: Univ. Arizona Press), 245
Baratta, G. A., & Palumbo, M. E. 1998, JOSAA, 15, 3076
Bergin, E. A., Melnick, G. J., Gerakines, P. A., Neufeld, D. A., & Whittet, D. C. B. 2005, ApJL, 627, L33
Bergin, E. A., Neufeld, D. A., & Melnick, G. J. 1998, ApJ, 499, 777
Bergin, E. A., Neufeld, D. A., & Melnick, G. J. 1999, ApJL, 510, L145
Billot, N., Morales-Calderón, M., Stauffer, J. R., Megeath, S. T., & Whitney, B. 2012, ApJL, 753, L35
Bohren, C. F., & Huffman, D. R. 1983, Absorption and Scattering of Light by Small Particles (New York: Wiley)
Boogert, A. C. A., Blake, G. A., & Tielens, A. G. G. M. 2002, ApJ, 577, 271
Boogert, A. C. A., Pontoppidan, K. M., Knez, C., et al. 2008, ApJ, 678, 985
Boogert, A. C. A., Pontoppidan, K. M., Lahuis, F., et al. 2004, ApJS, 154, 359
Bouwman, J., Ludwig, W., Awad, Z., et al. 2007, A&A, 476, 995
Charnley, S. B. 1997, ApJ, 481, 396
Cook, A. M., Whittet, D. C. B., Shenoy, S. S., et al. 2011, ApJ, 730, 124
Dartois, E. 2006, A&A, 445, 959
Dartois, E., Demyk, K., d'Hendecourt, L., & Ehrenfreund, P. 1999, A&A, 351, 1066
Davydov, A. S. 1962, Theory of Molecular Excitons (New York: McGraw-Hill)
D'Hendecourt, L. B., & Jourdain de Muizon, M. 1989, A&A, 223, L5
Draine, B. T., & Lee, H. M. 1984, ApJ, 285, 89
Dunham, M. M., & Vorobyov, E. I. 2012, ApJ, 747, 52
Ehrenfreund, P., Boogert, A. C. A., Gerakines, P. A., Tielens, A. G. G. M., & van Dishoeck, E. F. 1997, A&A, 328, 649
Ehrenfreund, P., Dartois, E., Demyk, K., & d'Hendecourt, L. 1998, A&A, 339, L17
Ehrenfreund, P., Kerkhof, O., Schutte, W. A., et al. 1999, A&A, 350, 240
Fischer, W. J., Megeath, S. T., Tobin, J. J., et al. 2012, ApJ, 756, 99
Fraser, H. J., Collings, M. P., McCoustra, M. R. S., & Williams, D. A. 2001, MNRAS, 327, 1165
Furlan, E., McClure, M., Calvet, N., et al. 2008, ApJS, 176, 184
Garrod, R. T., & Pauly, T. 2011, ApJ, 735, 15
Gatley, I., Becklin, E. E., Mattews, K., et al. 1974, ApJL, 191, L121
Gerakines, P. A., Schutte, W. A., Greenberg, J. M., & van Dishoeck, E. F. 1995, A&A, 296, 810
Gerakines, P. A., Whittet, D. C. B., Ehrenfreund, P., et al. 1999, ApJ, 522, 357
Hartmann, L., Boss, A., Calvet, N., & Whitney, B. 1994, ApJL, 430, L49
Hartmann, L., Calvet, N., & Boss, A. 1996, ApJ, 464, 387
Hartmann, L., & Kenyon, S. J. 1996, ARA&A, 34, 207
Higdon, S. J. U., Devost, D., Higdon, J. L., et al. 2004, PASP, 116, 975
Houck, J., Roellig, T. L., van Cleve, J., et al. 2004, ApJS, 154, 18
Hudgins, D. M., Sandford, S. A., Allamandola, L. J., & Tielens, A. G. G. M. 1993, ApJS, 86, 713
Ioppolo, S., van Boheemen, Y., Cuppen, H. M., van Dishoeck, E. F., & Linnartz, H. 2011, MNRAS, 413, 2281
Keesom, W. H., & Köhler, J. W. L. 1934, Phy, 1, 655
Kim, H. J., Evans, N. J., II, Dunham, M. M., Lee, J.-E., & Pontoppidan, K. M. 2012, ApJ, 758, 38

Knez, C., Boogert, A. C. A., Pontoppidan, K. M., et al. 2005, ApJL, 635, L145
Kryukova, E., Megeath, S. T., Gutermuth, R. A., et al. 2012, AJ, 144, 31
Markwardt, C. B. 2009, in ASP Conf. Ser. 411, Astronomical Data Analysis Software and Systems XVIII, ed. D. A. Bohlender, D. Durand, & P. Dowler (San Francisco, CA: ASP), 251
Mastrapa, R. M., Sandford, S. A., Roush, T. L., Cruikshank, D. P., & Dalle Ore, C. M. 2009, ApJ, 701, 1347
McKee, C. F., & Ostriker, E. C. 2007, ARA&A, 45, 565
Mennella, V., Palumbo, M. E., & Baratta, G. A. 2004, ApJ, 615, 1073
Menten, K. M., Reid, M. J., Forbrich, J., & Brunthaler, A. 2007, A&A, 474, 515
Mezger, P. G., Zylka, R., & Wink, J. E. 1990, A&A, 228, 95
Molinari, S., Swinyard, B., Bally, J., et al. 2010, A&A, 518, L100
Neufeld, D. A., & Hollenbach, D. J. 1994, ApJ, 428, 170
Noble, J. A., Congiu, E., Dulieu, F., & Fraser, H. J. 2012, MNRAS, 421, 768
Noble, J. A., Dulieu, F., Congiu, E., & Fraser, H. J. 2011, ApJ, 735, 121
Nummelin, A., Whittet, D. C. B., Gibb, E. L., Gerakines, P. A., & Chiar, J. E. 2001, ApJ, 558, 185
Oba, Y., Watanabe, N., Kouchi, A., Hama, T., & Pirronello, V. 2010, ApJL, 712, L174
Öberg, K. I., Boogert, A. C. A., Pontoppidan, K. M., et al. 2011, ApJ, 740, 109
Oliveira, J. M., van Loon, J. T., Chen, C.-H. R., et al. 2009, ApJ, 707, 1269
Ormel, C. W., Paszun, D., Dominik, C., & Tielens, A. G. G. M. 2009, A&A, 502, 845
Ossenkopf, V. 1993, A&A, 280, 617
Pontoppidan, K. M., Boogert, A. C. A., Fraser, H. J., et al. 2008, ApJ, 678, 1005
Pontoppidan, K. M., Fraser, H. J., Dartois, E., et al. 2003, A&A, 408, 981
Poteet, C. A., Megeath, S. T., Watson, D. M., et al. 2011, ApJL, 733, L32

Reipurth, B., & Aspin, C. 2010, in Evolution of Cosmic Objects through Their Physical Activity, ed. H. A. Harutyunian, A. M. Mickaelian, & Y. Terzian (Yerevan: Gitutyum), 19
Roser, J. E., Vidali, G., Manicò, G., & Pirronello, V. 2001, ApJL, 555, L61
Ruffle, D. P., & Herbst, E. 2001, MNRAS, 324, 1054
Satorre, M. Á., Domingo, M., Millán, C., et al. 2008, P&SS, 56, 1748
Seale, J. P., Looney, L. W., Chen, C.-H. R., Chu, Y.-H., & Gruendl, R. A. 2011, ApJ, 727, 36
Seiber, B. A., Smith, A. M., Wood, B. E., & Müller, P. R. 1971, ApOpt, 10, 2086
Terebey, S., Shu, F. H., & Cassen, P. 1984, ApJ, 286, 529
Tielens, A. G. G. M., & Hagen, W. 1982, A&A, 114, 245
Tielens, A. G. G. M., Tokunaga, A. T., Geballe, T. R., & Baas, F. 1991, ApJ, 381, 181
Tobin, J. J., Hartmann, L., Bergin, E., et al. 2012, ApJ, 748, 16
Tobin, J. J., Hartmann, L., Chiang, H.-F., et al. 2011, ApJ, 740, 45
Tobin, J. J., Hartmann, L., Looney, L. W., & Chiang, H.-F. 2010, ApJ, 712, 1010
van Broekhuizen, F. A., Groot, I. M. N., Fraser, H. J., van Dishoeck, E. F., & Schlemmer, S. 2006, A&A, 451, 723
Werner, M., Roellig, T. L., Low, F. J., et al. 2004, ApJS, 154, 1
White, D. W., Gerakines, P. A., Cook, A. M., & Whittet, D. C. B. 2009, ApJS, 180, 182
Whittet, D. C. B., Cook, A. M., Chiar, J. E., et al. 2009, ApJ, 695, 94
Whittet, D. C. B., Gerakines, P. A., Tielens, A. G. G. M., et al. 1998, ApJL, 498, L159
Whittet, D. C. B., Shenoy, S. S., Bergin, E. A., et al. 2007, ApJ, 655, 332
Williams, J. P., Plambeck, R. L., & Heyer, M. H. 2003, ApJ, 591, 1025
Zasowski, G., Kemper, F., Watson, D. M., et al. 2009, ApJ, 694, 459